*Progress in Photovoltaics: Research and Applications*

WILEY

PROGRESS IN PHOTOVOLTAICS

RESEARCH ARTICLE OPEN ACCESS

# Simulation Insights Into Enhanced Emitter Contact Passivation via LECO on Industrial TOPCon Solar Cells

Jiayu Xu[1] | Yun Qin[1] | Zhiyuan Zhang[1] | Wei Fan[1] | Wu Zhang[1] | Qun Liu[1] | Jiaji Lin[1] | Yuhao Cheng[2] | Ning Song[2] | Bram Hoex[2] | Lang Zhou[3,4] | Fa-Jun Ma[3,4,1,2]

[1]Laplace Renewable Energy Technology Co. Ltd., Shenzhen, Guangdong Province, P. R. China | [2]School of Photovoltaic and Renewable Energy Engineering, University of New South Wales, Sydney, New South Wales, Australia | [3]NCU-GQC Institute of PV-HE-ES Technology, Jiujiang, Jiangxi Province, P. R. China | [4]Institute of Photovoltaics, Nanchang University, Nanchang, Jiangxi Province, P. R. China

**Correspondence:** Fa-Jun Ma (f.ma@unsw.edu.au)

**Received:** 29 July 2025 | **Revised:** 14 March 2026 | **Accepted:** 17 March 2026

**Keywords:** contact passivation | contact resistivity | LECO | numerical simulation | TBC | TOPCon

## ABSTRACT

Recent progress in industrial tunneling oxide passivated contact (TOPCon) solar cells has demonstrated that laser-enhanced contact optimization (LECO) technology substantially reduces the emitter contact recombination current density ($J_{0e,metal}$), leading to a remarkable enhancement in cell efficiency. However, the physical mechanisms underlying this suppression remain insufficiently explored. This study employs advanced numerical simulations to systematically decode the interactions between firing conditions, LECO treatment, and doping dynamics. A process simulation reveals that the boron profile exhibits negligible deviation after a typical firing step, ruling out thermal redistribution as a contributor to $J_{0e,metal}$ suppression. Instead, lower peak firing temperatures promote localized, non-continuous contact morphologies. In a baseline 25.5% TOPCon solar cell, this partial metal contact ratio is quantified at 37.27%, directly correlating with diminished recombination losses. To mitigate contact resistivity ($\rho_c$), LECO complementarily rectifies underfired contacts by forming excellent Ag/Si contacts. These insights motivate a dual optimization strategy: (1) *dopant engineering* via selective emitter technology to maximize contact passivation while minimizing $\rho_c$ and (2) *partial metal contact ratio reduction* by tuning firing parameters, Ag paste composition, LECO energy density, etc., aiming for a 1% partial contact ratio without compromising $\rho_c$. Implementing this approach, the simulated cell efficiency improves from 25.5% to 26.07%, offering actionable guidelines for industrial TOPCon optimization. The strategy also suggests an alternative route for $J_{0e,metal}$ suppression, paving a viable path to elevate the efficiency of conventional TOPCon solar cells, enabling them to compete with more advanced double-sided and back-contact solar cells.

## 1 | Introduction

Tunneling oxide passivated contact (TOPCon) solar cells, a mainstream high-efficiency crystalline silicon (c-Si) technology, offer significant advantages over the passivated emitter and rear cell (PERC) technology in both device efficiency and cost control, garnering substantial attention in the photovoltaic sector [1]. These *n*-type TOPCon solar cells utilize a rear-side passivated contact technology incorporating polycrystalline silicon (poly-Si) atop an oxide layer, resulting in low contact resistance and minimal surface recombination, attributed to their superior carrier selectivity. This technology effectively mitigates the issue of rear metal–silicon interface recombination, enabling TOPCon solar cells to exhibit exceptional performance. However, a pivotal challenge for *n*-TOPCon solar cells in further enhancing conversion efficiency lies in the contact passivation between the front metal electrode and the boron (B)-doped $p^+$ emitter, suppressing both contact recombination and resistance.

The contact formation process in industrial production is generally carried out in a fast-firing belt furnace [2]. The silver (Ag) paste is applied on top of a passivation stack (e.g., $SiN_x$:H/$AlO_x$:H) using screen-printing technology. As the firing process occurs at temperatures exceeding 700°C, the glass frit within the paste locally etches away the passivation layers underneath the paste. This opening is necessary, which allows the Ag paste to be alloyed with Si, facilitating the creation of a low-resistive contact between the metal electrode and the emitter. However, it is not a trivial task to form high-quality contacts with the emitter. Various optimization strategies were implemented to address this issue, such as refining screen-printing processes and firing profiles [2, 3], improving paste compositions [4], optimizing passivation layers [5], and enhancing selective emitter (SE) doping levels under metal [6, 7]. These methods can significantly decrease contact resistance and minimize metal-induced recombination losses.

Recently, laser-enhanced contact optimization (LECO) technology has been gaining wide recognition in the photovoltaic industry [8–10]. It applies high-intensity laser pulses to solar cells under a constant high reverse voltage. Initially developed for repairing poorly fired solar cells [11], LECO technology has expanded to the study and implementation of PERC solar cells, evaluating its influence on the stability of industrial PERC modules [12]. In 2022, Fellmeth et al. investigated the effects of LECO on industrial TOPCon solar cells [13], discovering that this technology allows for the lower peak firing temperature and quite different Ag paste, thereby mitigating metal-induced recombination effects. Using single-diode model calculations, the potential increase in maximum open-circuit voltage ($V_{oc}$) was estimated to be 21 mV, leading to a 0.6% improvement in cell efficiency.

In 2024, Wu et al. conducted an extensive study, indicating that LECO technology provides a wider firing processing window and, in combination with an aluminum (Al)-free paste on the B-doped surface, significantly improves the reliability of TOPCon modules [14]. This approach facilitates the use of more economical materials in TOPCon modules, ultimately reducing the overall cost of solar power production. In the same year, Fan et al. [15] and Wang et al. [16] highlighted that special Al-free Ag pastes with reduced Pb content exhibit reduced corrosion. Lately, Chen et al. systematically explored the underlying mechanisms after achieving low contact resistivity ($\rho_c$) on emitters with medium, high, and ultra-high sheet resistance ($R_{sh}$) [17]. The performance enhancement of industrial TOPCon solar cells after LECO has traditionally been ascribed to substantial contact resistance reduction. Although impressively low emitter contact recombination current density ($J_{0e,metal}$), such as 206 fA/cm$^2$ [16] and 88 fA/cm$^2$ [18], has been quantified after LECO treatment, a comprehensive analysis of the $J_{0e,metal}$ reduction remains lacking.

This study provides fundamental insights into the mechanisms by which LECO suppresses metal-induced recombination through comprehensive experimental and numerical analysis. A primary objective is to investigate the relationship between $J_{0e,metal}$ and contact geometry, particularly the ratio of total contact width to finger width, as reduced peak firing temperatures produce localized, discontinuous contact formations. Our findings motivate an integrated optimization approach: (1) implementation of SE to simultaneously minimize $J_{0e,metal}$ and $\rho_c$ through heavy doping beneath contacts and (2) fine-tuning of contact architecture via optimization of firing conditions, Ag paste composition, LECO energy density, etc., aiming to establish a practical route to overcome $J_{0e,metal}$-limited performance in industrial production.

## 2 | Methodology

### 2.1 | Emitter Contact Passivation Evaluation

Emitter passivation quality is conventionally quantified using symmetrically boron-diffused and passivated *n*-type lifetime test structures, as illustrated in Figure 1a. The effective minority carrier lifetime ($\tau_{eff}$) of a sample is evaluated via established characterization techniques including quasi-steady-state photoconductance (QSSPC), Suns-$V_{oc}$, or photoluminescence (PL) [19–22], facilitating extraction of the emitter recombination current density ($J_{0e}$) typically at the excess

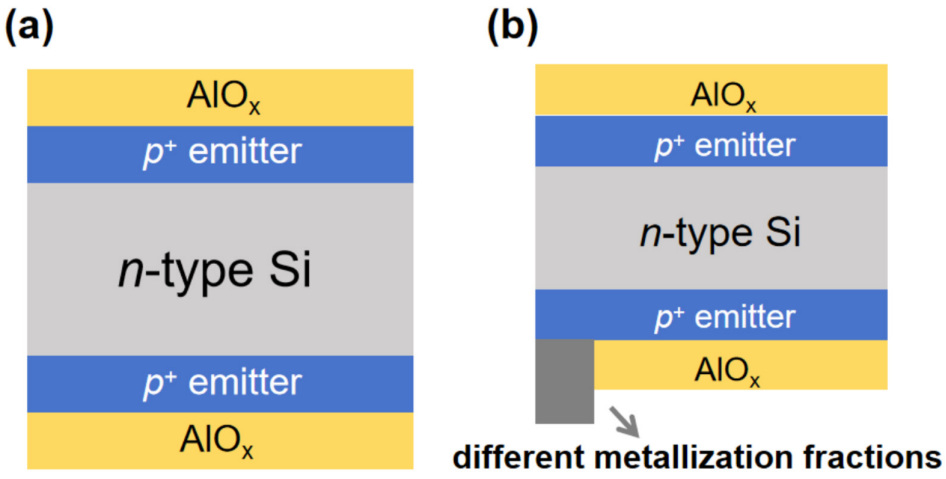


**FIGURE 1** | Schematic sketches of (a) a two-dimensional lifetime sample cross-section for determining the surface recombination velocity from $J_{0e,pass}$ and (b) $J_{0e,metal}$ test structures for determining $J_{0e,metal}$, featuring different metal contact fractions.

carrier density of $1\times10^{16}\,cm^{-3}$ using the Kane–Swanson method [23]. For passivated and metal-contacted emitters, $J_{0e}$ is conventionally distinguished as $J_{0e,pass}$ and $J_{0e,metal}$, respectively. For metal-contacted emitters, direct $J_{0e,metal}$ measurement presents challenges due to injection-level limitations and potential deviations in thin metal properties. To extract the $J_{0e,metal}$ reliably, an indirect method is employed instead on asymmetrically passivated lifetime samples with metal stripes, as depicted in Figure 1b, leveraging the linear dependence of the total $J_{0e}$ ($J_{0e,total}$) on its components:

$$J_{0e,total} = f_{mc}J_{0e,metal} + (1-f_{mc})J_{0e,pass} + J_{0e,pass} \quad (1)$$

where $f_{mc}$ stands for the fraction of the emitter surface covered by metal contacts, encompassing both the areas where a residual glass/$AlO_x$:H/$SiN_x$:H stack prevents direct metal–silicon contact and the areas where direct Ag/Si contact is formed. By varying $f_{mc}$ within a reasonable range, an accurate $J_{0e,metal}$ is extracted from the slope and intercept values of the $J_{0e,total}$ vs. $f_{mc}$ correlation [24, 25].

## 2.2 | TOPCon Simulation

The symmetrically passivated lifetime structure in Figure 1a was constructed in Sentaurus Technology Computer-Aided Design (TCAD) tool package [26] to carry out electrical simulations. The *n*-type substrate featured a thickness of 140 μm, a resistivity of 0.8 Ω·cm, and a Shockley–Read–Hall (SRH) [27] lifetime of 8.5 ms, according to the reference [16]. The Auger parameterization proposed by Niewelt et al. [28] together with the photon-recycling effect by Nguyen et al. [29] was implemented in the simulator. In addition, an optical simulation was conducted to generate the photogeneration profile required by electrical simulations under the Q-flash spectrum with an infrared pass filter [30]. The surface recombination velocity (SRV) of the area under the contact was set to be $10^7$ cm/s to assess $J_{0e,metal}$. Conversely, the SRV of the area beneath the passivation layers was determined from $J_{0e,pass}$.

When a metal forms full contact with the emitter, $J_{0e,metal}$ is entirely determined by the underlying boron profile, making it directly calculable from known dopant distributions. Yet, Fellmeth's research demonstrated that TOPCon solar cells employing LECO technology enabled firing at lower temperatures, reducing the peak firing temperature from 820°C to 780°C and decreasing $J_{0e,metal}$ monotonically from 1656 to 761 fA/cm² [13]. The metallization sequence is key to understanding the metallization–emitter contact in the context of LECO:

a. Boron source removal precedes screen-printing.
b. Firing etches through dielectric layers to establish Ag/Si contacts.
c. Complementary LECO treatment lowers contact resistance.

These insights suggest two possible mechanisms answering for the $J_{0e,metal}$ reduction:

a. Boron redistributes inside silicon due to high-temperature firing steps, e.g., a standard firing profile shown in Figure 2a, featuring a peak temperature of 740°C [31]. Notably, this peak temperature exceeds typical firing temperatures before LECO nowadays. Although LECO induces localized heating, its ultrashort duration (~1 s/wafer) [13] renders a negligible impact on B diffusion.

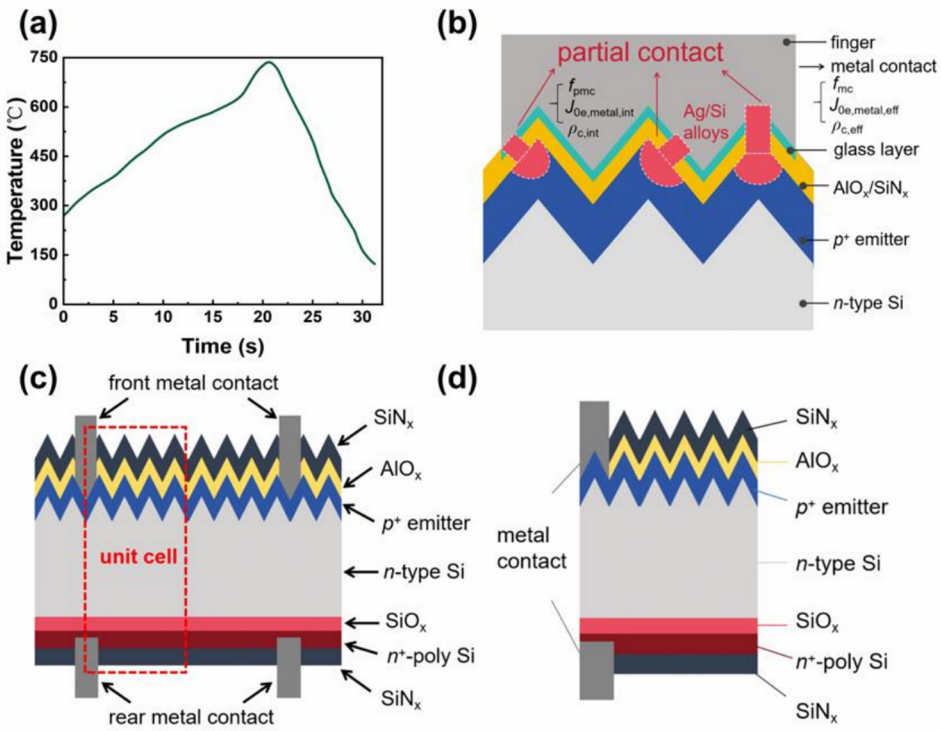


**FIGURE 2** | (a) A standard firing profile featuring a peak temperature of 740°C; (b) schematic sketches of partial metal contacts between emitter and finger; (c) schematic sketches of a 2D TOPCon solar cell cross-section; and (d) unit cell for simulation.

b. Silver paste only partially contacts the substrate due to insufficient peak firing temperature and duration, resulting in incomplete dielectric-layer etching as sketched in Figure 2b. A thin residual glass layer between Ag spikes and emitter further prevents full contact [17]. The recombination properties of the surface region under the glass layer remain unclear. Assuming equivalent passivation quality under dielectric and glass layers, $J_{0e,metal}$ reduction correlates with the partial metal contact ratio ($f_{pmc}$), defined as the ratio of metal area actually contacting the silicon emitter to the total area covered by the metallization finger.

## 2.3 | $J_{0e,metal}$ Suppression Investigation

To assess the first mechanism, a thermal diffusion simulation was carried out to check the difference in an industry-relevant boron profile before and after the firing process. For the second, it is necessary to define two terms to differentiate full and partial metal contacts. Analogous to the concept of intrinsic SRV and effective SRV [32], intrinsic $J_{0e,metal}$ ($J_{0e,metal,int}$) represents $J_{0e,metal}$ for full metal contact, and effective $J_{0e,metal}$ ($J_{0e,metal,eff}$) stands for weighted average $J_{0e,metal}$ for partial metal contact (refer to Figure 2b with schematic sketches of partial metal contacts):

$$J_{0e,metal,eff} = f_{pmc} J_{0e,metal,int} + (1 - f_{pmc}) J_{0e,pass} \tag{2}$$

Similarly, reported $\rho_c$ represents an effective $\rho_c$ ($\rho_{c,eff}$), related to the intrinsic $\rho_c$ ($\rho_{c,int}$) and $f_{pmc}$ by

$$\rho_{c,eff} = \frac{\rho_{c,int}}{f_{pmc}} \tag{3}$$

In metal–semiconductor contacts, the thermionic field emission mechanism dominates carrier transport, especially when the semiconductor is highly doped. An empirical relationship holds between $\rho_{c,int}$ and boron doping concentration ($N_A$) [33–35]:

$$\rho_{c,int} \propto \exp\left( \frac{\emptyset_B}{\sqrt{N_A} \coth\left( \frac{q\hbar}{2kT} \sqrt{\frac{N_A}{m_t^* \varepsilon_r \varepsilon_0}} \right)} \right) \tag{4}$$

where $\emptyset_B$ denotes the effective Schottky Barrier height, $k$ the Boltzmann constant, $T$ the temperature, $q$ the elementary charge, $\hbar$ the reduced Planck constant, $m_t^*$ the effective mass of the tunneling electron ($4.55 \times 10^{-31}$ kg), $\varepsilon_r$ the relative permittivity of Si (11.7), and $\varepsilon_0$ the absolute permittivity of free space ($8.85 \times 10^{-12}$ F/m).

The 25.5% TOPCon solar cell [16], as sketched in Figure 2b, was established in the simulator for meticulous investigation. A three-dimensional (3D) optical simulation was carried out, taking account of a front texture characterized by random upright pyramids and a rear surface modeled by a Phong exponent of 15 coupled with a broadband reflectivity of 88%. The antireflective coating stack consisted of an 80-nm $SiN_x$:H with a refractive index of 1.96 at 628 nm and a 3-nm hydrogenated aluminum oxide ($AlO_x$:H) [16]. The electrical simulation was conducted using the 2D structure, as depicted in Figure 2c. The 165 Ω/□ boron emitter profile was characterized by the electrochemical capacitance–voltage technique [16]. The UniSolar framework [36], featuring 11 user-friendly variables to define simulation procedures, was utilized to quickly carry out all these process, optical, and electrical simulations in this work.

We model the electrically active interface as discrete, direct Ag/Si contact points. The presence of the glass frit layer, although crucial for the firing process to etch the passivation stack, is assumed to have a negligible direct contribution to conductance. Glass layer conduction occurs via trap-assisted tunneling through nano-scale Ag particles embedded in the glass matrix. However, this mechanism contributes to the total current only when the glass layer is very thin (typically $<2$–5 nm). Consequently, the primary current path in our model is assumed to be through Ag/Si contacts.

## 2.4 | Industrial Boron Profiles Fitting

The emitter contact recombination is the dominant loss mechanism in the TOPCon cell [16]. In fact, the reported $J_{0e,metal}$ in the literature are $J_{0e,metal,eff}$ instead. According to Equation (2), $J_{0e,metal,eff}$ could be reduced by lowering both $J_{0e,metal,int}$ and $f_{pmc}$. The former can be accomplished by optimizing boron profiles and the latter by experimenting with the firing parameters, silver paste composition, LECO energy density, etc. To optimize the industrial boron profiles, 10 boron profiles were extracted from multiple sources [37–46], as plotted in Figure 3a,b. These profiles covered a wide range of industry-relevant boron profiles, consisting of boron peak concentration ($N_p$) from $4 \times 10^{18}$ to $10^{20}$ cm$^{-3}$, junction depths between 0.3 and 1.6 μm, and sheet resistance from 40 to 300 Ω/□. It is rational to find a mathematical formula to represent these profiles so that new industry-relevant boron profiles can be generated for subsequent evaluation. A boron diffusion profile is typically mathematically represented by a Gaussian distribution:

$$N(z) = N_p \cdot e^{-\left(\frac{z - z_p}{z_f}\right)^2} \tag{5}$$

where $N(z)$ is the depth-dependent concentration, $z$ is the depth below the substrate surface, $z_p$ is the depth of the peak concentration, and $z_f$ is the depth factor, which is determined by the junction depth. Due to the boron segregation effect between oxide and silicon, a boron depletion zone forms near the substrate surface. In order to capture this feature, we propose a double-Gaussian (DG) method, which employs another Gaussian distribution specifically for the depletion zone. The method is expressed mathematically as follows:

$$N(z) = \begin{cases} N_p \cdot e^{-\left(\frac{z - z_p}{z_{f1}}\right)^2}, & z < z_p \\ N_p \cdot e^{-\left(\frac{z - z_p}{z_{f2}}\right)^2}, & z \geq z_p \end{cases} \tag{6}$$

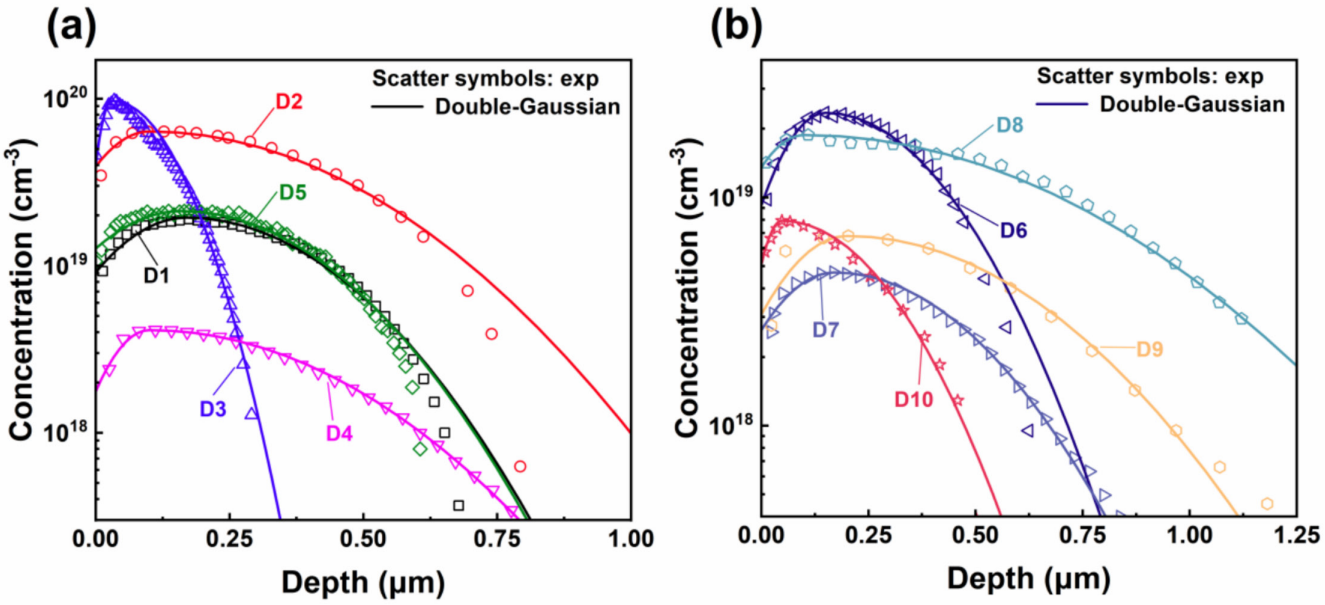


**FIGURE 3** | Various boron doping profiles pertinent to industrial applications, designated as D1–D10, have been meticulously extracted from multiple references [37–46]. Fitted by the double-Gaussian method, (a) D1–D5 and (b) D6–D10 are depicted for enhanced clarity and detailed examination.

**TABLE 1** | Boron profile fitting parameters.

| | $R_{sh}$ (Ω/□) | $N_p$ (cm$^{-3}$) | $z_p$ (μm) | $z_{f1}$ | $z_{f2}$ | Ref. |
|---|---|---|---|---|---|---|
| D1 | 117 | $1.94\times10^{19}$ | 0.17 | 0.1959 | 0.3148 | [37] |
| D2 | 39 | $6.36\times10^{19}$ | 0.12 | 0.1732 | 0.4151 | [38] |
| D3 | 95 | $9.71\times10^{19}$ | 0.03 | 0.0320 | 0.1311 | [39] |
| D4 | 324 | $4.12\times10^{18}$ | 0.10 | 0.1088 | 0.4274 | [40] |
| D5 | 112 | $2.12\times10^{19}$ | 0.16 | 0.2226 | 0.3131 | [41] |
| D6 | 109 | $2.35\times10^{19}$ | 0.15 | 0.1556 | 0.3181 | [42] |
| D7 | 269 | $4.70\times10^{18}$ | 0.17 | 0.2232 | 0.4040 | [43] |
| D8 | 69 | $1.88\times10^{19}$ | 0.10 | 0.1752 | 0.7535 | [44] |
| D9 | 152 | $6.79\times10^{18}$ | 0.20 | 0.2248 | 0.5433 | [45] |
| D10 | 322 | $7.91\times10^{18}$ | 0.048 | 0.0723 | 0.2966 | [46] |

These industrial boron profiles can be well represented by the DG method, as shown in Figure 3, and the corresponding fitting parameters required by Equation (6) are listed in Table 1.

An optimized boron profile with reduced $J_{0e,metal,int}$ was implemented under the front contact as the heavily doped emitter to form the SE structure, not only minimizing recombination at the metal–semiconductor interface but also enhancing carrier transport properties. The impact of $f_{pmc}$ reduction on the efficiency of TOPCon solar cells was systematically investigated. The simultaneous use of lower $J_{0e,metal,int}$ and $f_{pmc}$ was examined to demonstrate the synergistic potential of optimizing both contact design and emitter doping profiles to push the performance limit of industrial TOPCon solar cells.

## 3 | Results and Discussion

### 3.1 | Root Cause of $J_{0e,metal}$ Suppression

Fellmeth et al. showed that $J_{0e,metal}$ decreased from 1656 to 761 fA/cm$^2$ while the peak firing temperatures declined for the same boron emitter [13]. Wang et al. explored the effects of LECO by employing specialized silver paste (characterized by reduced lead content) on $J_{0e,metal,eff}$ and $\rho_{c,eff}$ [16]. Their findings revealed that the utilization of specialized silver paste decreased the line bulk resistivity from 3.56 to 2.60 μΩ·cm, whereas subsequent LECO treatment further decreased $\rho_c$ to approximately 0.91 mΩ·cm$^2$. Concurrently, a significant reduction in $J_{0e,metal}$ was observed, dropping to 206 fA/cm$^2$ for samples treated with LECO technology, compared to 503 fA/cm$^2$ for those subjected to conventional high-temperature firing.

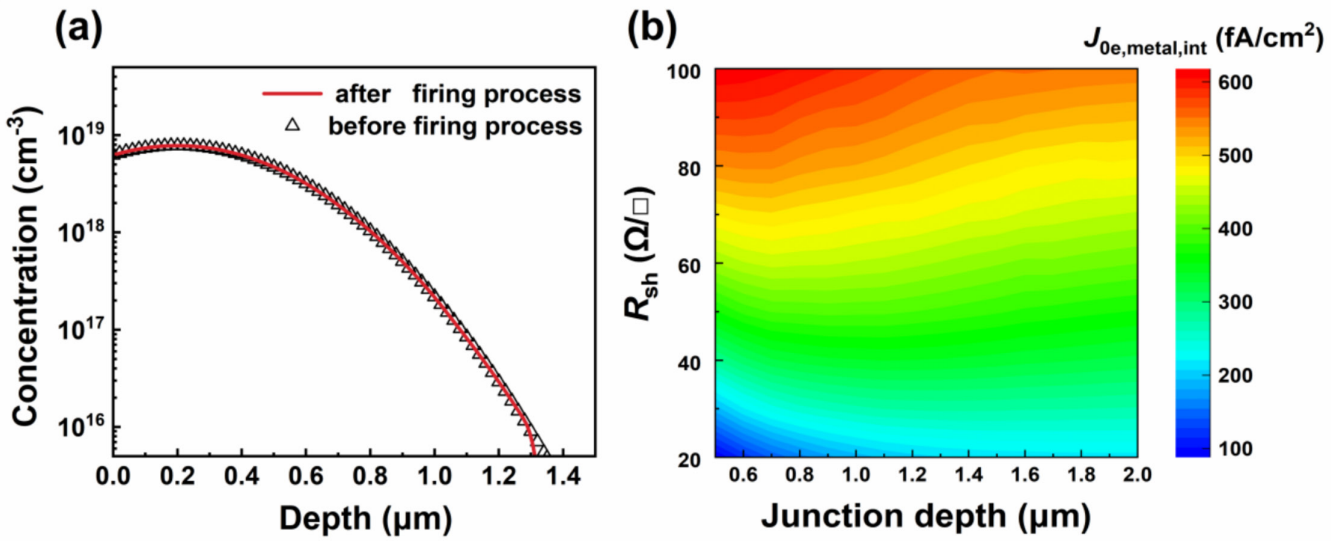


**FIGURE 4** | (a) Boron profile before the firing process and after the firing process, indicating that the impact of the annealing process on boron redistribution can be neglected; (b) a plot depicting the variation of $J_{0e,metal,int}$ as a function of depth ranging from 0.5 to 2 μm, featuring constant $R_{sh}$ of 20, 30, 40, 50, 60, 70, 80, 90, and 100 Ω/□.

**TABLE 2** | PCE, $V_{oc}$, short-circuit current density ($J_{sc}$), and fill factor (FF) of the baseline TOPCon solar cell from both experiment and simulation.

| Baseline | PCE (%) | $V_{oc}$ (mV) | $J_{sc}$ (mA/cm$^2$) | FF (%) |
|---|---|---|---|---|
| Wang et al. [16] | 25.50 | 723.40 | 41.86 | 84.05 |
| Simulation | 25.50 | 723.49 | 41.86 | 84.06 |

Process simulation based on the typical annealing time–temperature curve [47] in Figure 2a confirms that the boron profile [16] remains unchanged after firing, as illustrated in Figure 4a. According to the $\tau_{eff}$ simulation with a fully metallized structure, the corresponding $J_{0e,metal,int}$ was determined to be 735.4 fA/cm$^2$, much higher than 206 fA/cm$^2$ (after LECO) and also higher than 503 fA/cm$^2$ (as-fired). It is worth noting that the extracted $J_{0e,metal,eff}$ represents the lower limit, as in reality Ag typically penetrates at least a few tens of nanometers inside the emitter.

As such, those reported $J_{0e,metal}$ were $J_{0e,metal,eff}$, instead of $J_{0e,metal,int}$. The underlying mechanism for the decreased $J_{0e,metal,eff}$ can only be attributed to the reduced corrosiveness of the glass melt on the passivation layer at lower firing temperatures. The specialized Ag paste, which is Al-free and compatible with LECO technology, exhibits minimal penetration into the passivation layer during low-temperature firing. This process mitigates the damage to the emitter layer and the passivation layer. The localized high-temperature heating induced by the LECO technique facilitates the formation of bowl-shaped Ag/Si nano-alloys, which generate smaller corrosion pits compared to those formed during conventional high-temperature firing without LECO [16]. This structural modification reduces $f_{pmc}$ and, consequently, leads to a significant reduction in $J_{0e,metal,eff}$, as governed by Equation (2).

**TABLE 3** | Input parameters and values for the baseline TOPCon solar cell simulation.

| Parameters | Values |
|---|---|
| Temperature ($K$) | 298.15 |
| Front $f_{pmc}$ (%) | 37.27 |
| Front finger width (μm) | 22 |
| Front finger pitch (μm) | 1200 |
| Rear finger width (μm) | 30 |
| Front $\rho_{c,eff}$ (mΩ·cm$^2$) | 0.91 |
| Front $\rho_{c,int}$ (mΩ·cm$^2$) | 0.339 |
| Homogeneous emitter $R_{sh}$ (Ω/□) | 165 |
| Substrate thickness (μm) | 140 |
| Substrate resistivity (Ω·cm) | 0.9 |
| Substrate doping (cm$^{-3}$) | $5.46\times10^{15}$ |
| Substrate $J_{0,bulk}$ (fA/cm$^2$) | 5 |
| Substrate SRH lifetime (ms) | 8.5 |
| Oxide thickness (nm) | 1 |
| Poly-Si thickness (nm) | 70 |
| Poly-Si doping (cm$^{-3}$) | $2\times10^{20}$ |
| Front $J_{0e,pass}$ (fA/cm$^2$) | 6 |
| Front $J_{0e,metal,eff}$ (fA/cm$^2$) | 277.87 |
| Rear $J_{0r,pass}$ (fA/cm$^2$) | 4 |
| Rear $J_{0r,metal}$ (fA/cm$^2$) | 70 |
| Front electron and hole intrinsic SRV (cm/s) | 1688 |
| Rear electron and hole intrinsic SRV (cm/s) | 1638 |

Based on this understanding, optical and electrical simulations were conducted to replicate the baseline TOPCon cell from the experiment, with performance characteristics compared in Table 2. The simulated power conversion efficiency (PCE) and open-circuit voltage were 25.61% and 723.49 mV, respectively, whereas PCE was adjusted to be 25.5% by considering a lumped series resistance due to grid, and $f_{pmc}$ was fitted to be 37.27%. According to Equation (2), $J_{0e,metal,eff}$ was calculated to be 277.87 fA/cm$^2$ because $J_{0e,metal,int}$ and $J_{0e,pass}$ were 735.4 and 6 fA/cm$^2$, respectively. The simulated results are slightly different from the measurement, where $J_{0e,metal,eff}$ drops from 503 to 206 fA/cm$^2$ [16], corresponding to $f_{pmc}$ of 68.14% and 27.42%, respectively. According to Equation (3), $\rho_{c,int}$ was calculated to be 0.339 mΩ·cm$^2$ for the baseline simulation based on $\rho_{c,eff}$ and $f_{pmc}$ of 0.91 mΩ·cm$^2$ and 37.27%, respectively. Detailed input parameters for all variables were provided in Table 3 to replicate the baseline TOPCon.

### 3.2 | Doping Engineering

Variations in boron profiles and the corresponding $R_{sh}$ significantly influence $J_{0e,metal,int}$ due to field-effect passivation. Figure 4b illustrates the relationship between $J_{0e,metal,int}$ and varying junction depths (0.5–2 μm) for a constant $R_{sh}$ ranging from 20 to 100 Ω/□, where $z_p$ was fixed at 0.05 μm, with $N_p$, $z_{f1}$, and $z_{f2}$ being dependent outcomes. The results indicate that when $R_{sh}$ is low (≤ 50 Ω/□), $J_{0e,metal,int}$ gradually increases with depth and stabilizes as the depth approaches 2 μm. In contrast, when $R_{sh}$ is relatively high (> 50 Ω/□), $J_{0e,metal,int}$ exhibits a slightly downward trend before saturation. With a constant junction depth, $J_{0e,metal,int}$ always decreases monotonically with $R_{sh}$.

Industrial boron diffusion is carried out through thermal processes using tube furnaces. The boron doping concentration in the near-surface region initially rises to a peak value and subsequently decreases monotonically with increasing depth, and the peak active concentration typically remains below $10^{20}$ cm$^{-3}$. By employing the DG method, boron profiles that are close to reality can be obtained for the varying depth, which determines $z_{f2}$, with Equation (6) by fixing $N_p$, $z_p$, and $z_{f1}$ to $10^{20}$ cm$^{-3}$, 0.05 μm, and 0.151, respectively. The calculated $R_{sh}$ and $J_{0e,metal,int}$ of those profiles are plotted against the depth in Figure 5a. The results indicate that, with a constant peak concentration, $R_{sh}$ and $J_{0e,metal,int}$ decrease as junction depth increases. For shallow junction depths, $R_{sh}$ and $J_{0e,metal,int}$ decline rapidly. However, for deep junctions, the reduction in $R_{sh}$ and $J_{0e,metal,int}$ tends to plateau. Notably, at a depth of 2 μm, $J_{0e,metal,int}$ reaches its lowest value of about 213 fA/cm$^2$, with $R_{sh}$ = 20 Ω/□. Beyond this depth, $J_{0e,metal,int}$ increases gradually with depth due to enhanced Auger recombination associated with deep junctions. As those emitters are initially passivated, $J_{0e,pass}$ exhibits a monotonic increase with depth, as shown in Figure 5b. Based on Equation (2), $J_{0e,metal,eff}$ reaches its minimum value of 152 fA/cm$^2$ at the characteristic depth of 2 μm. The simulation results align with prior research, suggesting that optimizing the boron doping depth can effectively mitigate the interaction between metal contacts and minority carriers, suppressing $V_{oc}$ losses [37].

Unlike the homogeneous emitter (HE) used in the baseline TOPCon cell, the SE design effectively mitigates two critical issues: severe interfacial recombination and excessive contact resistance at the metal–semiconductor interface, by fabricating a highly doped emitter underneath the metal finger. The baseline TOPCon structure was modified to incorporate an SE design, which accurately replaced the lightly doped emitter ($R_{sh}$ = 165 Ω/□) with a heavily doped emitter ranging from 10 to 100 Ω/□ under contact, as sketched in Figure 6a. The same boron profiles used in Figure 5 were investigated to reveal their impact on cell performance, as demonstrated in Figure 6b–e. It is worth noting that thermionic field emission–induced metal–semiconductor contacts possess a contact resistivity that is 1–2 orders of magnitude lower than that of screen-printed contacts [48]. Theoretical $\rho_{c,int}$ is closely related to the active interfacial boron concentration. According to Equation (4), it was calculated to be $1.021 \times 10^{-5}$ and 0.12 mΩ·cm$^2$ for $10^{20}$ and $10^{18}$ cm$^{-3}$, respectively. Because $N_p$

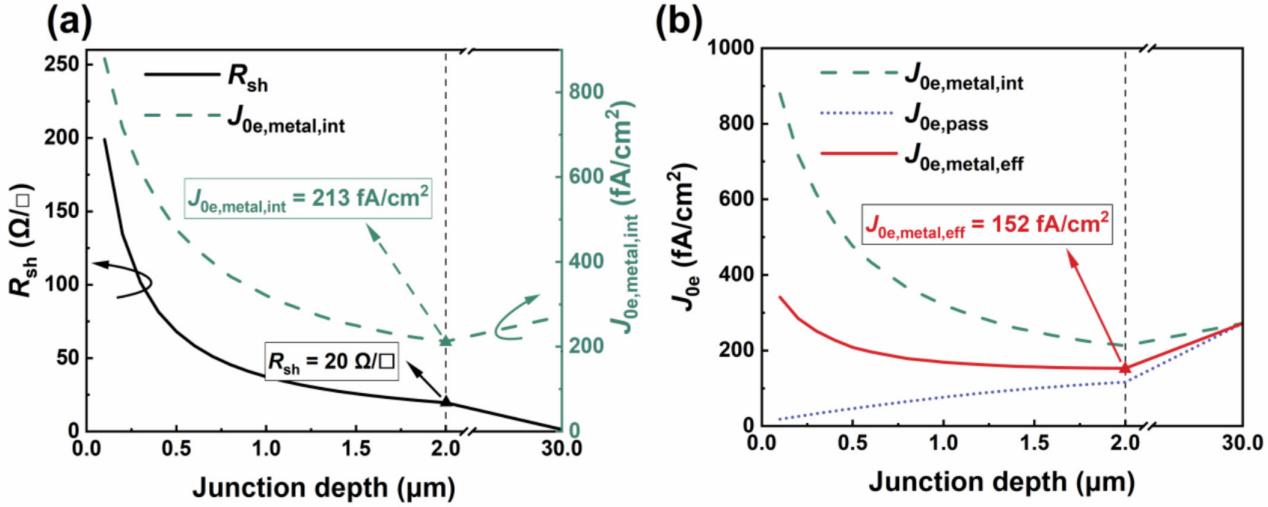


**FIGURE 5** | Junction depth–dependent (a) $R_{sh}$ and $J_{0e,metal,int}$; (b) $J_{0e,metal,int}$, $J_{0e,pass}$, and $J_{0e,metal,eff}$.

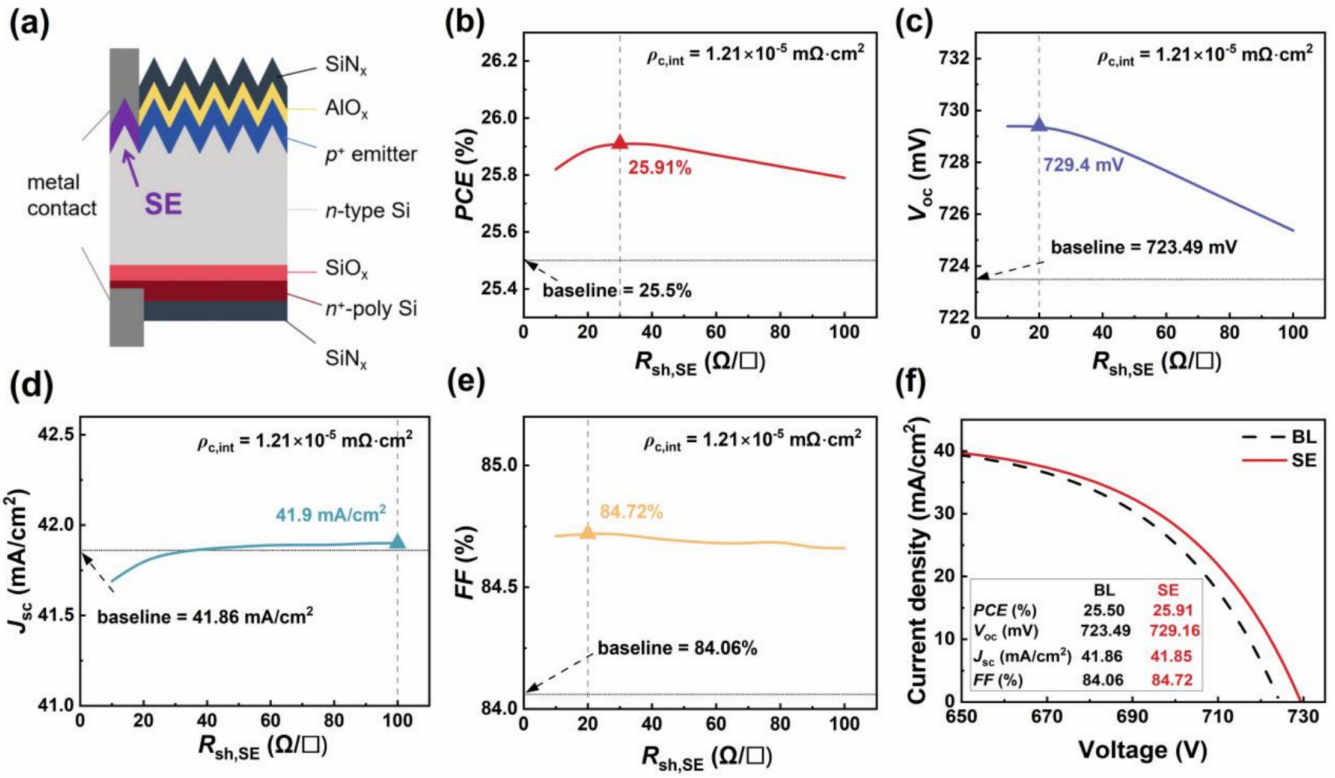


**FIGURE 6** | The baseline TOPCon solar cell with SE: (a) its schematic sketch of the unit cell and the impact of $R_{sh,SE}$ on (b) PCE, (c) $V_{oc}$, (d) $J_{sc}$, and (e) FF; and (f) its *J*–*V* curve with the $R_{sh,SE}$ of 30 Ω/□ as compared to that of the baseline.

is fixed to $10^{20}\,cm^{-3}$, $1.021\times10^{-5}\,m\Omega\cdot cm^2$ $\rho_{c,int}$ was applied to all emitters in simulations. The PCE of SE TOPCon solar cells initially rises rapidly before gradually declining as the SE sheet resistance ($R_{sh,SE}$) increases from 10 to 100 Ω/□. Concurrently, the $V_{oc}$ exhibits a downward trend with increasing $R_{sh,SE}$. Notably, the peak efficiency of 25.91% is achieved at $R_{sh,SE}=30\,\Omega/\square$, whereas the highest $V_{oc}$ of 729.4 mV occurs at $R_{sh,SE}=20\,\Omega/\square$, corresponding to the minimum $J_{0e,metal,eff}$ pinpointed in Figure 5. Figure 6f compares the current density–voltage (*J*–*V*) characteristics of the baseline and SE TOPCon with $R_{sh,SE}=30\,\Omega/\square$. By allocating high doping beneath metal contacts while preserving low doping elsewhere, SE optimizes the boron profile to enhance carrier transport, effectively suppressing $J_{0e,metal,int}$ and enhancing $V_{oc}$.

### 3.3 | Partial Metal Contact Ratio Reduction

To reduce $f_{pmc}$, it is imperative to optimize the firing parameters, silver paste composition, LECO energy density, etc. Firing temperature and duration can be fine-tuned so that the paste preserves dielectric passivation quality below the contact and barely etches through dielectric layers. As-fired solar cells should exhibit uniformly dark electroluminescence (EL) images, indicating a highly resistive contact. The paste can be modified to optimize its composition, viscosity, particle size, etc. In terms of LECO, the laser energy and reverse bias voltage can be adjusted so that the localized heat only facilitates the formation of local point contacts with good Ag/Si alloy, reducing both $f_{pmc}$ and $\rho_{c,eff}$. It is worth noting that the contact is modeled as a uniform, continuous area characterized by the $f_{pmc}$ ratio and that this simplification is appropriate for capturing the dominant area-dependent effects on $J_{0e,metal,eff}$ and $\rho_{c,eff}$.

The LECO-induced reduction in $J_{0e,metal,eff}$ not only encourages further process fine-tuning in the pursuit of lower $J_{0e,metal,eff}$ but also underscores the critical role of $f_{pmc}$ as a performance-determining factor in solar cell design. To quantitatively assess the impact of $f_{pmc}$ on cell efficiency and recombination losses, a comprehensive study was conducted to examine the $J_{0e,metal,eff}$ and cell performance across $f_{pmc}$ from 1% to 40%, as depicted in Figure 7. In these simulations, $\rho_{c,int}$ was assumed to be independent of $f_{pmc}$, and the predetermined value of $0.339\,m\Omega\cdot cm^2$ was applied. Although PCE improves moderately with decreasing $f_{pmc}$, it degrades abruptly below 14%, as shown in Figure 7a. The open pentagram marker represents the baseline TOPCon cell with 37.27% $f_{pmc}$. Although Figure 7b indicates that reduced $f_{pmc}$ simultaneously decreases $J_{0e,metal,eff}$ and increases $V_{oc}$, it is unable to fully explain the PCE trend, particularly given the nearly constant $J_{sc}$ shown in Figure 7c. Instead, the monotonic decrease in FF with $f_{pmc}$ in Figure 7d reveals the dominant role of rising $\rho_{c,eff}$, accounting for the observed PCE decline.

To evaluate the full potential of $f_{pmc}$ reduction, theoretical $\rho_{c,int}$ was calculated to be $1.06\times10^{-2}\,m\Omega\cdot cm^2$ and incorporated into simulations. As compared to the reference value of $0.339\,m\Omega\cdot cm^2$, PCE with theoretical $\rho_{c,int}$ increases all the way up to the peak value of 26.02% as $f_{pmc}$ decreases to 3%,

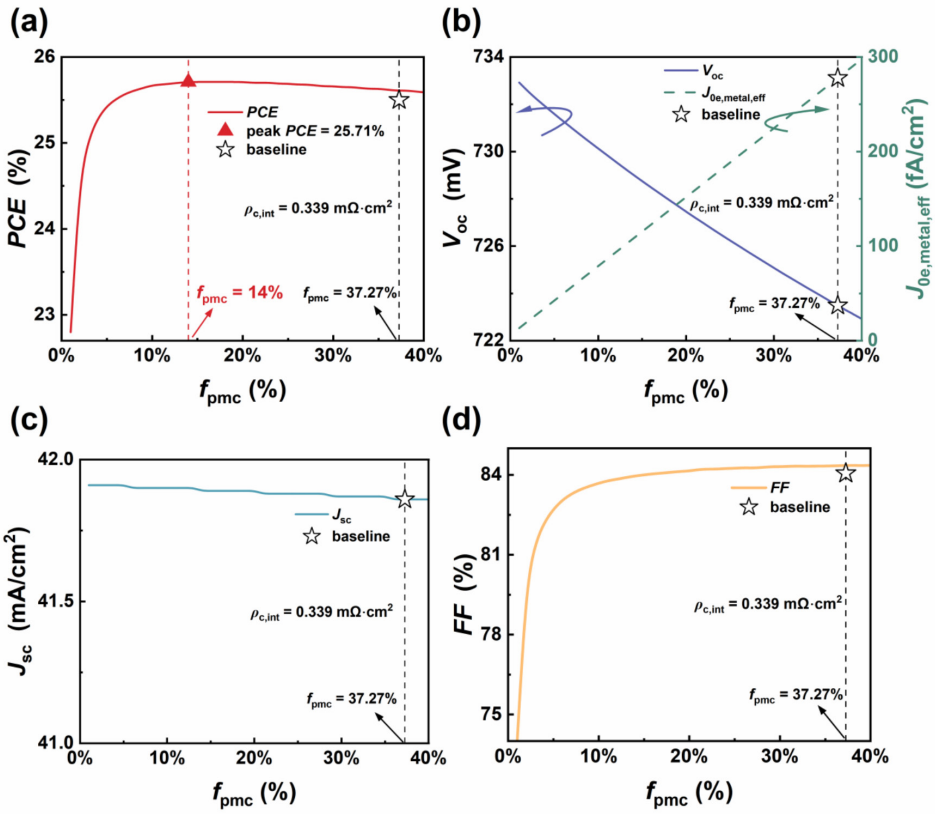


**FIGURE 7** | The impact of 1%–40% $f_{pmc}$ on (a) PCE, (b) $V_{oc}$ and $J_{0e,metal,eff}$, (c) $J_{sc}$, and (d) FF in baseline TOPCon cells with $\rho_{c,int} = 0.339\,m\Omega\cdot cm^2$.

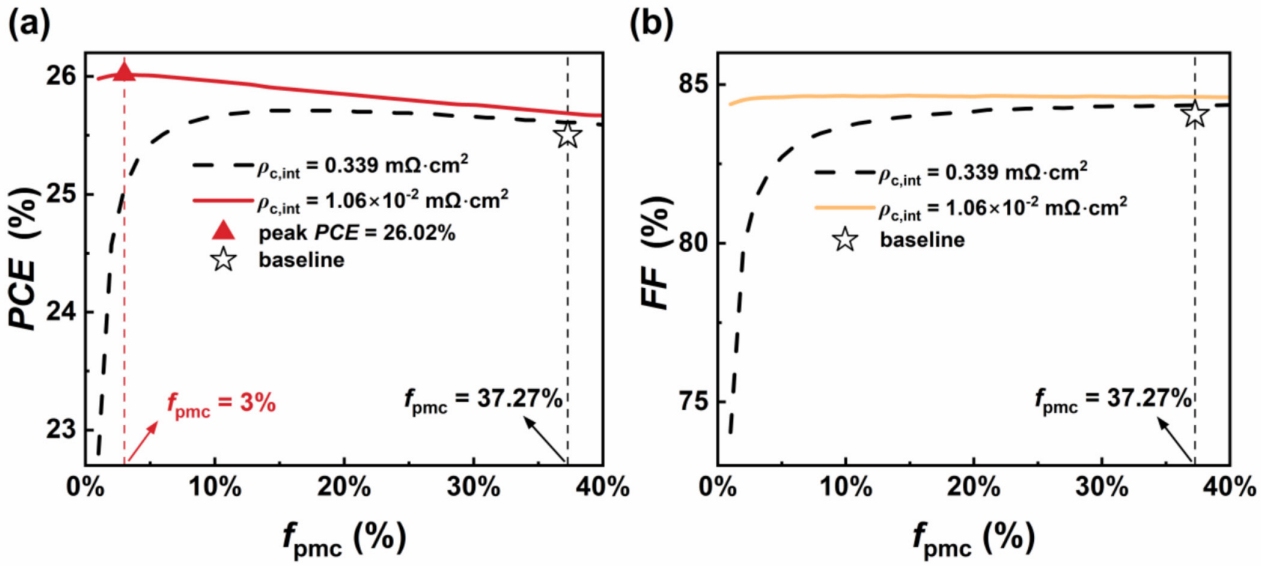


**FIGURE 8** | (a) PCE and (b) FF across 1%–40% $f_{pmc}$ for TOPCon solar cells with experimental ($0.339\,m\Omega\cdot cm^2$) and theoretical ($1.06\times10^{-2}\,m\Omega\cdot cm^2$) $\rho_{c,int}$.

as shown in Figure 8a. Because both configurations exhibit negligible differences in $V_{oc}$ and $J_{sc}$ (not shown), only FF is examined, and it is found to be stable down to 3% $f_{pmc}$, as depicted in Figure 8b. Therefore, the PCE improvement is driven exclusively by the rising $V_{oc}$ achieved through reduced $f_{pmc}$. Below the 3% $f_{pmc}$ threshold, the marginal PCE reduction results from FF degradation, indicating that the rising $\rho_{c,eff}$ outweighs the $V_{oc}$ enhancement.

### 3.4 | A Dual Optimization Strategy for TOPCon

Given that SE and $f_{pmc}$ reduction independently improve PCE, it is compelling to systematically assess their synergy. The SE structures employed industrially relevant boron diffusion profiles (Figure 3, $R_{sh}$ range: 39–152 Ω/□), whereas the HE (165 Ω/□) served as the TOPCon reference. Based on Equation (4), theoretical $\rho_{c,int}$ was calculated for these

emitters based on the peak doping concentration, as listed in Table 4. Meanwhile, $f_{pmc}$ was progressively decreased from 40% down to 1%. It is worth noting that the PCE improvements below only stemmed from $J_{0e,metal,eff}$ suppression. Additional gains may be realized by optimizing other losses like $J_{0e,pass}$.

**TABLE 4** | Industrial boron profiles with different theoretical $\rho_{c,int}$.

| | $R_{sh}$ (Ω/□) | $N_p$ ($cm^{-3}$) | $\rho_{c,int}$ (mΩ·$cm^2$) | Ref. |
|---|---|---|---|---|
| D1 | 117 | $1.94\times10^{19}$ | $2.04\times10^{-3}$ | [37] |
| D2 | 39 | $6.36\times10^{19}$ | $2.96\times10^{-5}$ | [38] |
| D5 | 112 | $2.12\times10^{19}$ | $1.69\times10^{-3}$ | [41] |
| D6 | 109 | $2.35\times10^{19}$ | $1.45\times10^{-3}$ | [42] |
| D8 | 69 | $1.88\times10^{19}$ | $2.08\times10^{-3}$ | [44] |
| D9 | 152 | $6.79\times10^{18}$ | $1.35\times10^{-2}$ | [45] |
| HE | 165 | $7.81\times10^{18}$ | $1.06\times10^{-2}$ | [16] |

Figure 9a illustrates the dependence of PCE on $R_{sh,SE}$ and $f_{pmc}$. As discussed earlier, the peak PCE reaches 26.02% for HE at 3% $f_{pmc}$. With the inclusion of SE, the maximum PCE is further enhanced to 26.07% at 1% $f_{pmc}$ and 117 Ω/□ $R_{sh,SE}$. Figure 9b reveals that the $J_{0e,metal,eff}$ can be further reduced by decreasing $f_{pmc}$. At 1% $f_{pmc}$, $J_{0e,metal,eff}$ declines as $R_{sh,SE}$ increases, reaching 20 fA/$cm^2$ at 117 Ω/□ $R_{sh,SE}$ and dropping to an exceptional 12 fA/$cm^2$ at 152 Ω/□. This value suggests that SE contact recombination is already the same as SE $J_{0e,pass}$. However, as seen in Figure 9c, $R_{sh,SE}$ has a significant influence on $\rho_{c,eff}$ at 1% $f_{pmc}$. Unlike $J_{0e,metal,eff}$, $\rho_{c,eff}$ increases monotonically with $R_{sh,SE}$, adversely affecting FF (not shown). Because the impact of $R_{sh,SE}$ on $J_{0e,metal,eff}$ is partially counterbalanced by its impact on $\rho_{c,eff}$, the peak PCE occurs at $f_{pmc}=1\%$ and $R_{sh,SE}=117$ Ω/□, where $J_{sc}$ also reaches its maximum. Once contact recombination is sufficiently suppressed through low $J_{0e,metal,eff}$ and $f_{pmc}$, $J_{0e,pass}$ emerges as the dominant loss mechanism. Consequently, the pursuit of ultimate efficiency

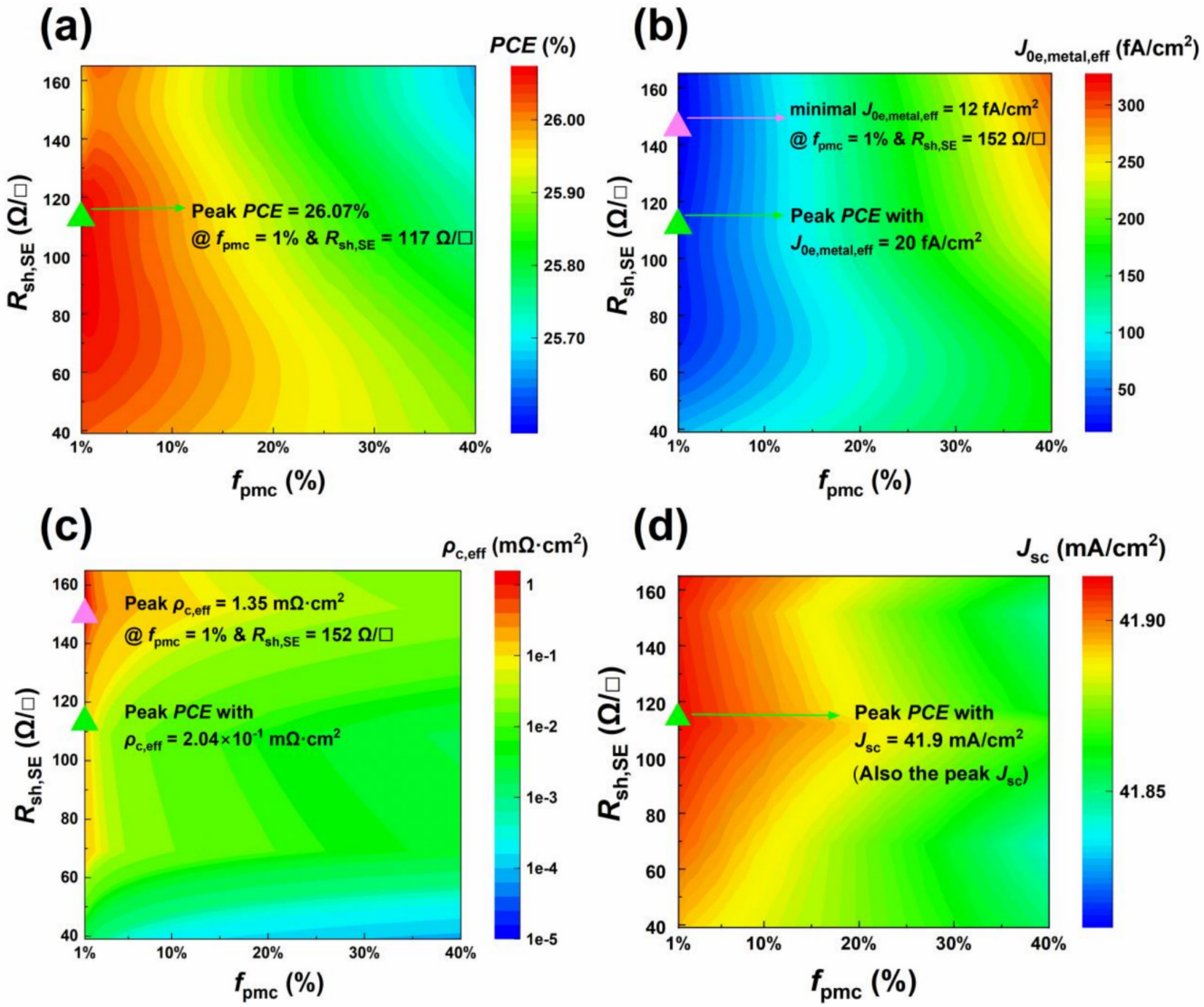


**FIGURE 9** | Synergistic effects of $R_{sh,SE}$ (39–165 Ω/□) and $f_{pmc}$ (1%–40%) on (a) PCE, (b) $J_{0e,metal,eff}$, (c) $\rho_{c,eff}$, and (d) $J_{sc}$ of the TOPCon solar cell.

**TABLE 5** | Optimization roadmap of TOPCon based on numerical simulations.

| Methods | PCE (%) | $V_{oc}$ (mV) | $J_{sc}$ (mA/cm$^2$) | FF (%) | $\rho_{c,int}$ (mΩ·cm$^2$) | $f_{pmc}$ (%) | $J_{0e,metal,eff}$ (fA/cm$^2$) |
|---|---|---|---|---|---|---|---|
| Baseline Exp (165 Ω/□) | 25.50 | 723.40 | 41.86 | 84.05 | 0.620 | 68.14 | 503 |
| Baseline (165 Ω/□) | 25.50 | 723.49 | 41.86 | 84.06 | 0.339 | 37.27 | 277.87 |
| SE (30 Ω/□) | 25.91 | 729.16 | 41.85 | 84.72 | $1.21\times10^{-5}$ | 37.27 | 159.71 |
| LECO (165 Ω/□) | 25.71 | 729.02 | 41.89 | 83.96 | 0.339 | 14 | 108.12 |
| LECO (165 Ω/□) | 26.02 | 732.21 | 41.91 | 84.58 | $1.06\times10^{-2}$ | 3 | 27.88 |
| SE + LECO (117 Ω/□) | 26.07 | 732.91 | 41.91 | 84.63 | $2.04\times10^{-3}$ | 1 | 20.47 |

necessitates further advancements in surface passivation to reduce $J_{0e,pass}$.

Table 5 outlines the optimization roadmap of the baseline TOPCon solar cell in this work, focusing on suppressing $J_{0e,metal,eff}$ and $\rho_{c,eff}$. The implementation of SE enhances doping concentration beneath the contact, reducing both $J_{0e,metal,int}$ and $\rho_{c,int}$. Meanwhile, contact optimization with LECO reduces $f_{pmc}$, linearly decreasing the contribution of metal–semiconductor recombination to $J_{0e,metal,eff}$. However, this also increases $\rho_{c,eff}$, creating a trade-off between these two effects. Although HE with LECO is the mainstream approach in industrial TOPCon production, our findings reveal that combining LECO and SE can further enhance PCE by simultaneously suppressing $J_{0e,metal,eff}$ and $\rho_{c,eff}$. Nevertheless, this dual optimization demands precise control over the doping process, the firing process, careful selection of paste materials, optimized LECO parameters, and innovative design strategies. As the technology matures, this approach is anticipated to drive further advancements in high-efficiency industrial TOPCon cells. Moreover, this strategy presents an alternative pathway for conventional TOPCon $J_{0e,metal,eff}$ suppression.

## 4 | Conclusions

This study systematically investigated the key factors influencing emitter contact recombination losses. The findings reveal that the primary mechanism behind reduced $J_{0e,metal,eff}$ is the minimized corrosion of the passivation layer by the glass melt at lower firing temperatures, rather than boron redistribution during metallization. The use of low firing temperature and specialized Ag paste combined with LECO technology significantly suppresses both $J_{0e,metal,eff}$ and $\rho_{c,eff}$ by forming localized Ag/Si nano-alloys. Doping engineering plays a crucial role in optimizing emitter performance. An SE design with industrially relevant boron profiles effectively reduces $J_{0e,metal,int}$ and $\rho_{c,int}$, achieving a peak efficiency of 25.91% at $R_{sh,SE} = 30\,\Omega/\square$. Further analysis demonstrates that reducing $f_{pmc}$ enhances $V_{oc}$ by lowering $J_{0e,metal,eff}$, but it also degrades FF due to an increasing $\rho_{c,eff}$, especially beyond a threshold (3%). Theoretical calculations suggest that PCE can reach 26.02% at 3% $f_{pmc}$ with ideal $\rho_{c,int}$ ($1.06\times10^{-2}$ mΩ·cm$^2$). The synergistic application of SE and $f_{pmc}$ reduction further boosts PCE, achieving a record 26.07% efficiency at 1% $f_{pmc}$ and 117 Ω/□ $R_{sh,SE}$. At this optimum condition, $J_{0e,metal,eff}$ drops to 20 fA/cm$^2$, nearly matching the passivated emitter recombination. Whereas higher $R_{sh,SE}$ further suppress $J_{0e,metal,eff}$ (e.g., 12 fA/cm$^2$), they also increase $\rho_{c,eff}$, necessitating a trade-off between $J_{0e,metal,eff}$ and $\rho_{c,eff}$.

Notably, this study focuses solely on $J_{0e,metal,eff}$ suppression; higher PCE gains are possible through additional improvements. These findings highlight the importance of a dual optimization approach, fine-tuning both doping profiles and $f_{pmc}$ to boost TOPCon solar cell efficiency. Future work should explore advanced metallization techniques and alternative passivation schemes to further minimize $J_{0e,metal,eff}$ while maintaining low $\rho_{c,eff}$, pushing the efficiency of industrial TOPCon cells beyond 26%. Moreover, this study implies an alternative approach for suppressing $J_{0e,metal,eff}$, offering a competitive pathway for the conventional TOPCon solar cells, enabling them to compete with more advanced double-sided and back-contact solar cells.

### Author Contributions

**Jiayu Xu:** writing – original draft, software, visualization, investigation, formal analysis, data curation. **Yun Qin:** writing – review and editing. **Zhiyuan Zhang:** writing – review and editing. **Wei Fan:** writing – review and editing. **Wu Zhang:** writing – review and editing. **Qun Liu:** writing – review and editing. **Jiaji Lin:** writing – review and editing. **Yuhao Cheng:** writing – review and editing. **Ning Song:** writing – review and editing. **Bram Hoex:** writing – review and editing. **Lang Zhou:** writing – review and editing. **Fa-Jun Ma:** writing – review and editing, software, visualization, investigation, formal analysis, methodology, supervision, project administration, conceptualization.


### Acknowledgments

This work was supported by Laplace Renewable Energy Technology Co. Ltd., a global leading supplier of photovoltaic equipment and solutions. Laplace does not accept responsibility for the views, information, or advice expressed in this research. Jiayu Xu would like to sincerely acknowledge Siwen Gu from Changzhou University for generously sharing details of the baseline TOPCon solar cell. Fa-Jun Ma gratefully acknowledges the sponsorship by the 2024 "Gan Po Jun Cai" Program and the Key Project (20244BAB28012) of the Natural Science Foundation of Jiangxi Province. All simulations were performed on the UNSW Compute Cluster Katana (DOI: 10.26190/669X-A286). Open access publishing facilitated by University of New South Wales, as part of the Wiley - University of New South Wales agreement via the Council of Australasian University Librarians

## Funding

This study was supported by the Natural Science Foundation of Jiangxi Province (20244BAB28012).

## Conflicts of Interest

The authors declare no conflicts of interest.

## Data Availability Statement

The Tar/GZip files for the baseline TOPCon simulations are accessible under 07tpl/02pub/2025Xu-LECO on the UniSolar GitHub repository.

## References

1. F. Feldmann, M. Bivour, C. Reichel, M. Hermle, and S. W. Glunz, "Passivated Rear Contacts for High-Efficiency *n*-Type Si Solar Cells Providing High Interface Passivation Quality and Excellent Transport Characteristics," *Solar Energy Materials & Solar Cells* 120 (2014): 270–274, https://doi.org/10.1016/j.solmat.2013.09.017.

2. M. Li, J. Wong, E. C. Wang, et al., "Predictive Simulation Framework for Boron Diffused $p^+$ Layer Optimization: Sensitivity Analysis of Boron Tube Diffusion Process Parameters of Industrial *n*-Type Silicon Wafer Solar Cells," *Solar Energy Materials & Solar Cells* 189, no. 9 (2019): 63–74, https://doi.org/10.1016/j.solmat.2018.09.019.

3. S. M. Ahmad, C. S. Leong, K. Sopian, and S. H. Zaidi, "Role of Firing Temperature, Sheet Resistance, and Contact Area in Contact Formation on Screen-Printed Metal Contact of Silicon Solar Cell," *Journal of Electronic Materials* 47, no. 3 (2018): 2120–2134, https://doi.org/10.1007/s11664-017-6022-7.

4. P. Padhamnath, A. Khanna, N. Balaji, et al., "Progress in Screen-Printed Metallization of Industrial Solar Cells With $SiO_x$/Poly-Si Passivating Contacts," *Solar Energy Materials & Solar Cells* 218, no. 31 (2020): 110751, https://doi.org/10.1016/j.solmat.2020.110751.

5. Y.-Y. Huang, Y. W. Ok, K. Madani, et al., "~23% Rear Side Poly-Si/$SiO_2$ Passivated Silicon Solar Cell With Optimized Ion-Implanted Boron Emitter and Screen-Printed Contacts," *Solar Energy Materials & Solar Cells* 230 (2021): 111183, https://doi.org/10.1016/j.solmat.2021.111183.

6. W. Lin, D. Chen, C. Liu, et al., "Green-Laser-Doped Selective Emitters With Separate $BBr_3$ Diffusion Processes for High-Efficiency *n*-Type Silicon Solar Cells," *Solar Energy Materials and Solar Cells* 210 (2020): 110462, https://doi.org/10.1016/j.solmat.2020.110462.

7. D. Ding, Z. du, R. Liu, et al., "Laser Doping Selective Emitter With Thin Borosilicate Glass Layer for *n*-Type TOPCon c-Si Solar Cells," *Solar Energy Materials & Solar Cells* 253 (2023): 112230, https://doi.org/10.1016/j.solmat.2023.112230.

8. E. Krassowski, B. Jaeckel, M. Pander, D. Daßler, and S. Malik, "Assessing the Long-Term Stability of Laser Enhanced Contact Optimization (LECO) Treated PERC Cells in PV Modules by Extended Indoor and Outdoor Durability Tests," *EPJ Photovoltaics* 14, no. 13 (2023): 1–8, https://doi.org/10.1051/epjpv/2023004.

9. S. Großer, E. Krassowski, S. Swatek, H. Zhao, and C. Hagendorf, "Microscale Contact Formation by Laser Enhanced Contact Optimization," *IEEE Journal of Photovoltaics* 12, no. 1 (2022): 26–30, https://doi.org/10.1109/JPHOTOV.2021.3129362.

10. R. Mayberry, "Laser Enhanced Contact Optimization (LECO) and LECO-Specific Pastes—A Novel Technology for Improved Cell Efficiency," 36th European Photovoltaic Solar Energy Conference and Exhibition (2019).

11. C. Kim, J. W. Choi, S. Choi, et al., "Effects of Current-Injection Firing With Ag Paste in a Boron Emitter," *Scientific Reports* 6 (2016): 21553, https://doi.org/10.1038/srep21553.

12. E. Krassowski, B. Jaeckel, U. Zeller, et al., "Reliability Evaluation of Photovoltaic Modules Fabricated From Treated Solar Cells by Laser-Enhanced Contact Optimization Process," *Solar RRL* 6, no. 5 (2022): 2100537(1–8), https://doi.org/10.1002/solr.202100537.

13. T. Fellmeth, H. Höffler, S. Mack, et al., "Laser-Enhanced Contact Optimization on iTOPCon Solar Cells," *Progress in Photovoltaics: Research and Applications* 30, no. 12 (2022): 1393–1399, https://doi.org/10.1002/pip.3598.

14. X. Wu, X. Wang, W. Yang, et al., "Enhancing the Reliability of TOPCon Technology by Laser-Enhanced Contact Firing," *Solar Energy Materials & Solar Cells* 271 (2024): 112846, https://doi.org/10.1016/j.solmat.2024.112846.

15. Y. Fan, S. Zou, Y. Zeng, et al., "Investigation of the Ag–Si Contact Characteristics of Boron Emitters for *n*-Tunnel Oxide-Passivated Contact Solar Cells Metallized by Laser-Assisted Current Injection Treatment," *Solar RRL* 8, no. 13 (2024): 2400268, https://doi.org/10.1002/solr.202400268.

16. Q. Wang, K. Guo, S. Gu, W. Huang, W. Wu, and J. Ding, "Investigation on Effects of the Laser-Enhanced Contact Optimization Process With Ag Paste in a Boron Emitter for *n*-TOPCon Solar Cell," *Progress in Photovoltaics: Research and Applications* 33, no. 2 (2024): 294–308, https://doi.org/10.1002/pip.3854.

17. S. Chen, C. Guo, Z. Liu, et al., "Mechanisms and Strategies for Laser-Enhanced Contact Optimization in Tunnel Oxide Passivating Contact Solar Cells With Ultra-High Sheet Resistance Emitters," *Chemical Engineering Journal* 513 (2025): 162979, https://doi.org/10.1016/j.cej.2025.162979.

18. X. Wang, J. Yuan, X. Wu, et al., "Higher-Efficiency TOPCon Solar Cells in Mass Production Enabled by Laser-Assisted Firing: Advanced Loss Analysis and Near-Term Efficiency Potential," *Progress in Photovoltaics: Research and Applications* 33, no. 7 (2025): 771–781, https://doi.org/10.1002/pip.3921.

19. P. Zheng, J. Yang, Z. Wang, et al., "Detailed Loss Analysis of 24.8% Large-Area Screen-Printed *n*-Type Solar Cell With Polysilicon Passivating Contact," *Cell Reports Physical Science* 2, no. 10 (2021): 100603, https://doi.org/10.1016/j.xcrp.2021.100603.

20. T. Fellmeth, A. Born, A. Kimmerle, F. Clement, D. Biro, and R. Preu, "Recombination at Metal-Emitter Interfaces of Front Contact Technologies for Highly Efficient Silicon Solar Cells," *Energy Procedia* 8 (2011): 115–121, https://doi.org/10.1016/j.egypro.2011.06.111.

21. V. Shanmugam, T. Mueller, A. G. Aberle, and J. Wong, "Determination of Metal Contact Recombination Parameters for Silicon Wafer Solar Cells by Photoluminescence Imaging," *Solar Energy* 118 (2015): 20–27, https://doi.org/10.1016/j.solener.2015.05.010.

22. D. Ananthanarayanan, J. Wong, E. C. Wang, N. Chen, J. W. Ho, and A. G. Aberle, "Determination of Metal-Induced Recombination of *n*-Type Bifacial Si Solar Cells Using Special Print Patterns," *IEEE Journal of Photovoltaics* 9, no. 3 (2019): 643–651, https://doi.org/10.1109/JPHOTOV.2019.2903177.

23. D. E. Kane and R. M. Swanson, "Measurement of the Emitter Saturation Current by a Contactless Photoconductivity Decay Method," in *Conference Record of the IEEE Photovoltaic Specialists Conference* (IEEE, 1985), 578–583.

24. Q. Wang, H. Peng, S. Gu, et al., "High-Efficiency *n*-TOPCon Bifacial Solar Cells With Selective Poly-Si Based Passivating Contacts," *Solar Energy Materials & Solar Cells* 259 (2023): 112458, https://doi.org/10.1016/j.solmat.2023.112458.

25. Q. Wang, B. Gao, W. Wu, K. Guo, W. Huang, and J. Ding, "Effects on Metallization of $n^+$-Poly-Si Layer for *n*-Type Tunnel Oxide Passivated Contact Solar Cells," *Materials* 17, no. 11 (2024): 2747, https://doi.org/10.3390/ma17112747.

26. "Sentaurus TCAD," Synopsys Inc., Sunnyvale, CA, 2023, accessed September 10, 2023, https://www.synopsys.com/manufacturing/tcad.html.

27. W. Shockley and W. T. Read, "Statistics of the Recombinations of Holes and Electrons," *Semiconductor Devices: Pioneering Papers* 46 (1991): 62–69, https://doi.org/10.1142/9789814503464_0002.

28. T. Niewelt, B. Steinhauser, A. Richter, et al., "Reassessment of the Intrinsic Bulk Recombination in Crystalline Silicon," *Solar Energy Materials & Solar Cells* 235 (2022): 111467, https://doi.org/10.1016/j.solmat.2021.111467.

29. H. T. Nguyen, S. C. Baker-Finch, and D. MacDonald, "Temperature Dependence of the Radiative Recombination Coefficient in Crystalline Silicon From Spectral Photoluminescence," *Applied Physics Letters* 104, no. 11 (2014): 112105, https://doi.org/10.1063/1.4869295.

30. J. S. Swirhun, R. A. Sinton, M. K. Forsyth, and T. Mankad, "Contactless Measurement of Minority Carrier Lifetime in Silicon Ingots and Bricks," *Progress in Photovoltaics: Research and Applications* 19, no. 3 (2011): 313–319, https://doi.org/10.1002/pip.1029.

31. Z. Liu, J. Li, J. Tang, and Y. Zhang, "Effect of Firing Process on Electrical Properties and Efficiency of *n*-TOPCon Solar Cells," *Solar Energy* 267 (2024): 112205, https://doi.org/10.1016/j.solener.2023.112205.

32. Y. Rosenwaks, Y. Shapira, and D. Huppert, "Evidence for Low Intrinsic Surface-Recombination Velocity on *p*-Type InP," *Physical Review B: Condensed Matter* 44 (1991): 13097–13100, https://doi.org/10.1103/PhysRevB.44.13097.

33. S. M. Sze and K. K. Ng, "Part II: Device Building Blocks, Ch. 3.6 'Ohmic Contact," in *Physics of Semiconductor Devices* (Wiley, 2006), https://doi.org/10.1002/0470068329.

34. P. Padhamnath, N. Nampalli, A. Khanna, B. Nagarajan, A. G. Aberle, and S. Duttagupta, "Progress With Passivation and Screen-Printed Metallization of Boron-Doped monoPoly™ Layers," *Solar Energy* 231 (2022): 8–26, https://doi.org/10.1016/j.solener.2021.11.015.

35. A. Y. C. Yu, "Electron Tunneling and Contact Resistance of Metal-Silicon Contact Barriers," *Solid State Electronics* 13, no. 2 (1970): 239–247, https://doi.org/10.1016/0038-1101(70)90056-0.

36. F. -J. Ma, S. Wang, C. Yi, et al., "A Collaborative Framework for Unifying Typical Multidimensional Solar Cell Simulations—Part I. Ten Common Simulation Steps and Representing Variables," *Progress in Photovoltaics: Research and Applications* 32, no. 5 (2024): 330–345, https://doi.org/10.1002/pip.3779.

37. Q. Wang, W. Wu, Y. Li, et al., "Impact of Boron Doping on Electrical Performance and Efficiency of *n*-TOPCon Solar Cell," *Solar Energy* 227 (2021): 273–291, https://doi.org/10.1016/j.solener.2021.08.075.

38. J. Hong, X. Liu, J. Ge, et al., "Superb Improvement of Boron Doping in Selective Emitter for TOPCon Solar Cells via Boron-Doped Silicon Paste," *Solar Energy* 247 (2022): 115–122, https://doi.org/10.1016/j.solener.2022.10.031.

39. A. Richter, J. Benick, and M. Hermle, "Boron Emitter Passivation With $Al_2O_3$ and $Al_2O_3/SiN_x$ Stacks Using ALD $Al_2O_3$," *IEEE Journal of Photovoltaics* 3, no. 1 (2013): 236–245, https://doi.org/10.1109/JPHOTOV.2012.2226145.

40. X. Li, Q. Q. Wang, X. Dong, et al., "Optimization of Efficiency Enhancement of TOPCon Cells With Boron Selective Emitter," *Solar Energy Materials & Solar Cells* 263 (2023): 112585, https://doi.org/10.1016/j.solmat.2023.112585.

41. Y. Zhou, K. Tao, A. Liu, et al., "Study of Boron Diffusion for $p^+$ Emitter of Large Area *n*-Type TOPCon Silicon Solar Cells," *Applied Physics A* 126, no. 9 (2020): 1–10, https://doi.org/10.1007/s00339-020-03851-5.

42. Q. Wang, K. Guo, L. Yuan, et al., "Boron Tube Diffusion Process Parameters for High-Efficiency *n*-TOPCon Solar Cells With Selective Boron Emitters," *Solar Energy Materials & Solar Cells* 253 (2023): 112231, https://doi.org/10.1016/j.solmat.2023.112231.

43. W. Chen, W. Liu, Y. Yu, Y. Ke, and Y. Wan, "Study on Selective Emitter Fabrication Through an Innovative Pre-Diffusion Process for Enhanced Efficiency in TOPCon Solar Cells," *Progress in Photovoltaics: Research and Applications* 32, no. 3 (2024): 199–211, https://doi.org/10.1002/pip.3766.

44. M. Peng, Q. Wang, M. Zhang, et al., "Optimization of Boron Depletion for Boron-Doped Emitter of *n*-Type TOPCon Solar Cells," *Materials Science in Semiconductor Processing* 178 (2024): 108424, https://doi.org/10.1016/j.mssp.2024.108424.

45. J. Hong, J. Sun, X. Liu, et al., "High-Efficiency TOPCon Solar Cells With Laser-Assisted Localized Boron Doping via Silicon Paste," *IEEE Journal of Photovoltaics* 14, no. 4 (2024): 583–591, https://doi.org/10.1109/JPHOTOV.2024.3380461.

46. X. Liu, J. Sun, Y. Huang, et al., "High-Efficiency TOPCon Solar Cell With Superior $p^+$ and $p^{++}$ Layer via One-Step Processing," *Solar Energy* 271 (2024): 112448, https://doi.org/10.1016/j.solener.2024.112448.

47. H. Wang, S. Ma, M. Zhang, F. Lan, H. Wang, and J. Bai, "Effects of Screen Printing and Sintering Processing of Front Side Silver Grid Line on the Electrical Performances of Multi-Crystalline Silicon Solar Cells," *Journal of Materials Science: Materials in Electronics* 28, no. 16 (2017): 11934–11949, https://doi.org/10.1007/s10854-017-7003-6.

48. T. G. Allen, J. Bullock, X. Yang, A. Javey, and S. De Wolf, "Passivating Contacts for Crystalline Silicon Solar Cells," *Nature Energy* 4, no. 11 (2019): 914–928, https://doi.org/10.1038/s41560-019-0463-6.